

pubs.acs.org/NanoLett Letter

# **Engineering Magnetic Nanoclusters for Highly Efficient Heating in Radio-Frequency Nanowarming**

Zuyang Ye, Youyi Tai, Zonghu Han, Sangmo Liu, Michael L. Etheridge, Jacqueline L. Pasek-Allen, Chaitanya Shastry, Yun Liu, Zhiwei Li, Chen Chen, Zhongxiang Wang, John C. Bischof, Jin Nam, and Yadong Yin\*



Cite This: Nano Lett. 2024, 24, 4588-4594



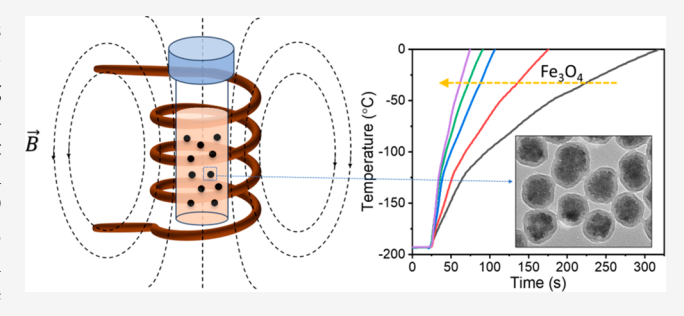
ACCESS

Metrics & More

Article Recommendations

s Supporting Information

**ABSTRACT:** Effective thawing of cryopreserved samples requires rapid and uniform heating. This is achievable through nanowarming, an approach that heats magnetic nanoparticles by using alternating magnetic fields. Here we demonstrate the synthesis and surface modification of magnetic nanoclusters for efficient nanowarming. Magnetite (Fe<sub>3</sub>O<sub>4</sub>) nanoclusters with an optimal diameter of 58 nm exhibit a high specific absorption rate of 1499 W/g Fe under an alternating magnetic field at 43 kA/m and 413 kHz, more than twice that of commercial iron oxide cores used in prior nanowarming studies. Surface modification with a permeable resorcinol-formaldehyde resin (RFR) polymer layer significantly



enhances their colloidal stability in complex cryoprotective solutions, while maintaining their excellent heating capacity. The  $Fe_3O_4@$  RFR nanoparticles achieved a high average heating rate of 175 °C/min in cryopreserved samples at a concentration of 10 mg Fe/mL and were successfully applied in nanowarming porcine iliac arteries, highlighting their potential for enhancing the efficacy of cryopreservation.

KEYWORDS: iron oxide nanoparticles, surface modification, colloidal stability, magnetic heating, biocompatibility, nanowarming

ryopreservation, the preservation of biological systems at ultralow temperatures, is a crucial technology enabling long-term storage and transportation of living cells, tissues, and organs without compromising their structural integrity and biological functions.  $^{1-3}$  The ability to cryopreserve complex tissues and whole organs holds immense potential for applications across various biomedical fields, including transplantation and regenerative medicine.<sup>4-6</sup> However, successful cryopreservation and subsequent rewarming of large tissues and organs remain challenging due to the risk of destructive ice crystal formation and cracking during cooling and rewarming. Vitrified cryopreservation is an approach that uses the aid of high-molarity cryoprotective solutions to reach a cryopreserved state without significant ice crystallization. However, slow heating from the vitrified state leads to ice recrystallization, causing mechanical damage to cells and tissues, while uneven heating induces thermal stresses, resulting in cracks and structural damage.<sup>7-9</sup> Therefore, technological advances enabling rapid and uniform heating during rewarming are imperative for improving post-thaw viability of cryopreserved biological samples. 10-13

Magnetic nanoparticles have emerged as a promising platform for nanowarming, a technique that leverages these nanoparticles to generate heat under an alternating magnetic field, thereby facilitating rapid and uniform heating of cryopreserved biological samples. 14-17 Their potential to overcome the limitations of traditional convective rewarming methods has been demonstrated across tissues and organs, including rat hearts, livers, and kidneys. While previous work mainly focused on establishing the fundamental principles, feasibility, and initial protocols for nanowarming, the work used commercially available iron oxide nanoparticle cores and rational optimization of intrinsic nanoparticle properties such as size, assembly states, and surface coating to boost their heating performance remains less investigated. 14-27

In this work, we report the rational design of magnetic nanoclusters with optimized size and functional surface coating for efficient nanowarming applications. Monodisperse Fe<sub>3</sub>O<sub>4</sub> nanoclusters were synthesized through a robust metal-ion-steered solvothermal approach with tunable sizes ranging from 37 to 400 nm, allowing for systematic investigation of size-

Received: February 8, 2024
Revised: April 2, 2024
Accepted: April 4, 2024
Published: April 8, 2024





dependent heating performance. Nanoclusters with an average diameter of 58 nm demonstrated superior heating performance (normalized to mass), with a specific absorption rate (SAR) of 1499 W/g Fe, more than double the performance of commercial EMG308 iron oxide nanoparticles. Further, one of the additional challenges of nanowarming applications is the need to retain colloidal stability in the complex solutions used in cryopreservation. These solutions are high molarity (often up to 9 M+) and contain a variety of organic solvents, polymers, sugars, alcohols, and salts. Surface modification of magnetic nanoclusters with a resorcinol-formaldehyde resin (RFR) polymer layer significantly enhanced their long-term colloidal stability in the studied cryoprotective agent (CPA) solution without compromising their heating capacity. These iron oxide-polymer core-shell nanoparticles exhibited excellent heating performance, achieving rapid heating of 175 °C/min in cryopreserved samples at a concentration of 10 mg Fe/mL. Cytotoxicity tests suggested biocompatibility of the nanoclusters, which were successfully applied for the nanowarming of porcine iliac arteries. This work presents a promising material platform for advancing magnetic nanoparticle-based nanowarming techniques through rational optimization of nanoparticle properties.

The synthesis of size-tunable magnetic iron oxide nanoclusters was achieved through a solvothermal method, with ethylene glycol (EG) as both the solvent and reducing agent and FeCl<sub>3</sub> as the precursor for Fe<sub>3</sub>O<sub>4</sub>. Adding ethylenediamine (en) generated an alkaline environment, facilitating the formation of Fe(OH)<sub>3</sub> and its subsequent conversion to Fe<sub>3</sub>O<sub>4</sub>. Ni<sup>2+</sup> was introduced as a competing complexing agent to accelerate the release of Fe<sup>2+</sup> from Fe(en)<sub>2</sub>, effectively modulating the nucleation and growth kinetics of Fe<sub>3</sub>O<sub>4</sub> nanoclusters. By adjusting the molar ratio of Ni<sup>2+</sup> to Fe<sup>3+</sup> between 0:1 and 2:1, the average size of Fe<sub>3</sub>O<sub>4</sub> nanoclusters could be readily tuned from 400 to 37 nm (Figure 1 and Figure S1). The X-ray diffraction (XRD) patterns of the Ni-doped

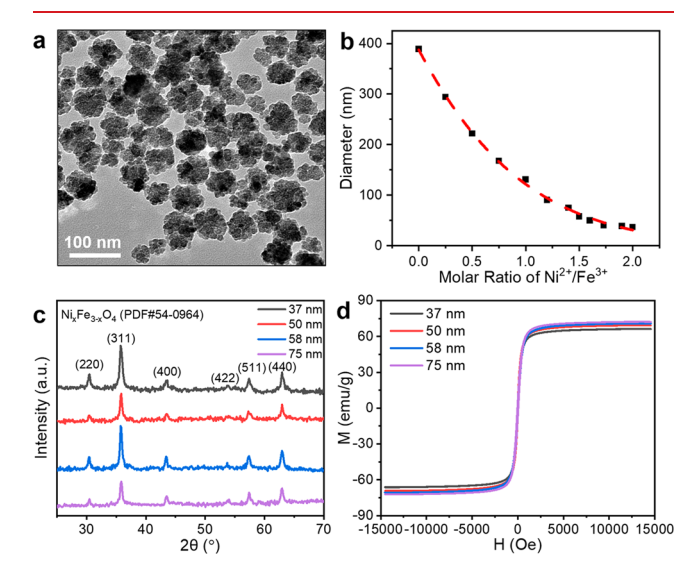


**Figure 1.** (a) TEM image of typical  $Fe_3O_4$  nanoclusters with an average diameter of 58 nm. (b) Dependence of average diameters of  $Fe_3O_4$  nanoclusters on the molar ratio of  $Ni^{2+}/Fe^{3+}$  in the precursor solution. The red dashed curve represents the Boltzmann fitting between the diameter and molar ratio of  $Ni^{2+}/Fe^{3+}$ . (c, d) XRD patterns (c) and magnetic hysteresis loops (d) of  $Fe_3O_4$  nanoclusters of different sizes.

iron oxide nanoclusters revealed well-defined peaks corresponding to the face-centered-cubic spinel phase  $\mathrm{Ni}_x\mathrm{Fe}_{3-x}\mathrm{O}_4$  (Figure 1c), indicating the high purity of the products. Given the nominal Ni content exhibited in the nanoclusters as revealed by inductively coupled plasma optical emission spectroscopy (ICP-OES) shown in Table S1, they are referred to as  $\mathrm{Fe}_3\mathrm{O}_4$  nanoclusters for simplicity in the following discussions. Table S1 summarizes the average crystal sizes of the nanoparticles calculated by the Scherrer formula. The crystal sizes increased with nanoparticle sizes.

The magnetic properties of Fe<sub>3</sub>O<sub>4</sub> nanoclusters were characterized by magnetic hysteresis measurements. As shown in Figure 1d, all samples exhibit ferrimagnetic behavior and display typical S-shaped M-H curves. The saturation magnetization  $(M_s)$  and coercivity  $(H_c)$  values increase with particle and crystal sizes, reaching 72.3 emu/g and 45.8 Oe, respectively. This observation aligns with studies on the sizedependent magnetic properties of Fe<sub>3</sub>O<sub>4</sub> nanoparticles.<sup>29–32</sup> The increase in crystal size reduced the surface spin disorder, thereby enhancing the ferromagnetism of the samples. Additionally, the increase in the nanocluster diameter indicated a larger number of nanocrystal agglomerates. The interaction between crystallites contributed to the increase in the  $M_{\rm s}$  value. The  $M_s$  value of Fe<sub>3</sub>O<sub>4</sub> nanoclusters was higher than that of typical Fe<sub>3</sub>O<sub>4</sub> nanospheres, <sup>33,34</sup> which is advantageous for subsequent magnetic heating applications.

The heating performance of magnetic nanoparticles, a critical parameter for nanowarming applications, was evaluated by placing a 2 mL Eppendorf tube containing 1 mL of the prepared sample within a water-cooled copper coil (see the Supporting Information for additional details) subjected to an alternating magnetic field at 43 and 413 kHz. The temperature change of each sample was monitored by a fiber optic temperature sensor, and the heating profiles are plotted in Figure 2a. Samples were insulated during heating, and heating in a solution without nanoparticles was subtracted for baseline heating. Nanoclusters of 58 nm diameter demonstrated optimal heating performance, increasing the solution temperature from 25 to 58 °C within 30 s. The optimal heating performance is contingent upon a balance between the increased saturation magnetization and the nanoparticle agglomeration induced during heating. With particle diameters of less than 58 nm, the domain size increased along with the sample size, elevating the saturation magnetization and the heating rate.<sup>35,36</sup> However, when the sample size exceeded 58 nm, while the domain size remained constant around 23 nm based on XRD data, it is possible that more iron oxide nanocrystals were present in random orientations, which could potentially impede magnetic heating efficiency due to the intraaggregate magnetic dipolar interactions. 37-39 The higher saturation magnetization and coercivity led to stronger attractive interactions between particles, making them more likely to agglomerate under the external magnetic field, which was unfavorable for nanowarming applications (Figure S2).

The SAR, a parameter that quantifies the thermal power generated by magnetic nanoparticles, is defined as the power absorbed per unit mass of Fe. It can be calculated by the equation

$$SAR = \frac{\rho C_{p}}{[Fe]} \times \frac{\Delta T}{\Delta t}$$

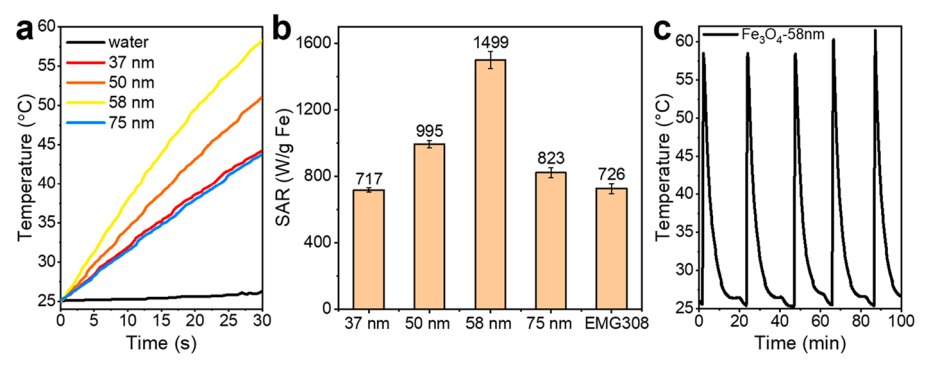
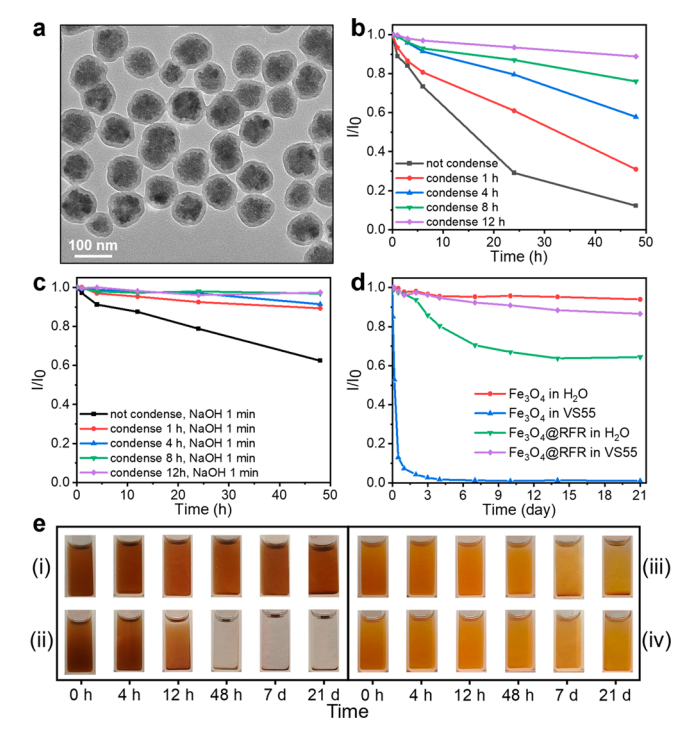


Figure 2. (a, b) Example heating profiles (a) and average specific absorption rate (SAR) (b) of Fe<sub>3</sub>O<sub>4</sub> nanoclusters of various sizes in water under an alternating magnetic field (at 413 kHz and 43 kA/m). (c) Cyclic heating performance of 58 nm Fe<sub>3</sub>O<sub>4</sub> nanoclusters.

where  $\rho$  and  $C_{\rm p}$  are the density and specific heat capacity of the solution, respectively, [Fe] is the concentration of Fe in the sample, and  $\frac{\Delta T}{\Delta t}$  is the heating rate of the solution measured over an adiabatic range of heating. As shown in Figure 2b, the SAR value of the sample initially increased and then decreased with an increase in the particle size. At a particle diameter of 58 nm, the optimal SAR value reached 1499 W/g Fe, exceeding the performance of commercial EMG308 iron oxide nanoparticles used in prior nanowarming work by more than 2-fold. The SAR values remained consistent within the measured concentration range, as shown in Table S2. Additionally, the cycling experiment suggested that the sample was stable and could avoid agglomeration during heating (Figure 2c).

Another crucial factor for nanowarming applications is the colloidal stability of nanoparticles in CPAs.<sup>25</sup> CPAs are compounds designed to protect cryopreserved biological samples from freezing damage caused by ice crystal formation. VS55, a widely used CPA that has been investigated for cryopreservation of tissues or organs, comprises organic solvents, sugars, and various inorganic salts, as listed in Table S3.<sup>42</sup> While as-synthesized magnetic nanoclusters modified with poly(acrylic acid) exhibited excellent colloidal stability in water, they were susceptible to aggregation and sedimentation in CPA solutions due to elevated ionic strength and insufficient electrostatic repulsion between particles. Moreover, these nanoparticles aggregated quickly under the alternating magnetic field, inhibiting uniform dispersion in the solution and thus compromising their heating performance (Figure S3).

Besides electrostatic repulsion, increasing the steric hindrance between nanoparticles is another effective strategy to prevent the agglomeration of colloidal particles. To achieve this, we modified the surface of Fe<sub>3</sub>O<sub>4</sub> nanoclusters with a layer of RFR polymer (Figure 3a and Figure S4). RFR, a commonly used resin polymer, can be easily coated on nanoparticle surfaces to serve as a steric barrier and impart good biocompatibility.  $^{43-46}$  We monitored the colloidal stability of the nanoparticles by using UV-vis absorption spectroscopy. As shown in Figure S5, the extinction peak intensity of nanoparticles without RFR coating in VS55 solution gradually diminished over time and was reduced to one-tenth of its initial value within 24 h. This result suggested that the particles precipitated, and thus, the concentration decreased. In contrast, the decay rate of the extinction peak significantly slowed after the RFR coating, indicating improved colloidal stability.



**Figure 3.** (a) TEM image of a typical sample of  $Fe_3O_4@RFR$  nanoparticles. (b, c) Time-dependent absorption peak intensity changes of different  $Fe_3O_4@RFR$  nanoparticles in VSS5 with various condensation times before (b) and after (c) 1 min of NaOH treatment. (d, e) Long-term stability test (d) and digital images (e) of aqueous dispersions of  $Fe_3O_4$  in  $H_2O$  (i) and VSS5 (ii), and  $Fe_3O_4$ @RFR in  $H_2O$  (iii) and VSS5 (iv).

We further investigated the effect of the RFR coating with different condensation times on the colloidal stability of Fe<sub>3</sub>O<sub>4</sub>@RFR nanoparticles, as exhibited in Figure 3b. Increased condensation of the RFR polymer leads to a higher degree of cross-linking, making the polymer network denser and more rigid.<sup>47</sup> This enhanced rigidity amplified the steric hindrance between nanoparticles, effectively reducing the tendency of them to aggregate. As a result, when the condensation time increased, the colloidal stability of the sample improved. Fe<sub>3</sub>O<sub>4</sub>@RFR samples condensed for 12 h showed roughly a 10% loss in peak intensity after being dispersed in VS55 for 48 h, indicating a significant improvement in stability compared to the uncoated samples. In addition, studies have shown that NaOH treatment can enhance the permeability of RFR.<sup>48</sup> For all Fe<sub>3</sub>O<sub>4</sub> samples of

various sizes, the colloidal stability was considerably improved after RFR coating and a 1 min NaOH treatment (Figure 3c). In this case, NaOH removed lower cross-linked oligomers within the RFR polymer network, facilitating the penetration of solvent molecules into the inner layer of RFR. Consequently, the interaction between internal hydroxyl groups and solvent molecules was strengthened, thereby stabilizing nanoparticles. RFR coating was instrumental in ensuring the long-term stability of  ${\rm Fe_3O_4}$  nanoclusters in CPA solution, enabling the samples to maintain good dispersion for over 3 weeks (Figure 3d, e and Figure S6). These findings underscore the potential of this surface modification approach for creating robust, stable nanoparticles for various applications in the field of nanomedicine and biotechnology.

To elucidate the impact of RFR modification on the heating performance of magnetic nanoparticles, we measured the SAR value of Fe<sub>3</sub>O<sub>4</sub>@RFR in both water and VS55, as shown in Figure 4a. Compared to the results without RFR modification

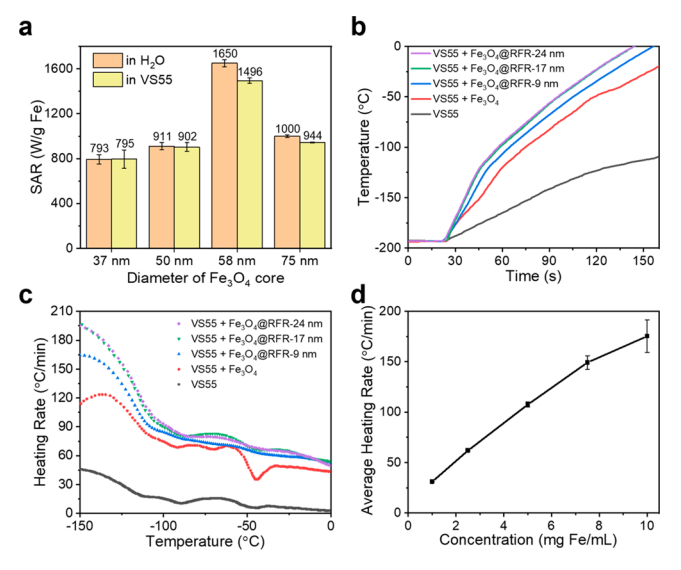


Figure 4. (a) SAR measurement (at 413 kHz, 43 kA/m) of Fe $_3O_4$ @ RFR nanoparticles with different core diameters in water or VS55. (b, c) The heating profile (b) and heating rate (c) of 58 nm Fe $_3O_4$  nanoparticles coated with RFR shells of different thicknesses starting from cryogenic temperatures. The Fe concentration of samples is 3 mg/mL. (d) The average heating rate of Fe $_3O_4$ @RFR (core 58 nm, shell 17 nm) at different concentrations, calculated between  $\sim$ -100 and -40 °C.

(Figure 2b), Fe<sub>3</sub>O<sub>4</sub> nanoclusters of different sizes maintained high SAR values after being coated with an RFR layer of approximately 10 nm in thickness. This observation suggests that the RFR layer of an appropriate thickness does not impede the heating performance or thermal conduction properties of the magnetic nanoparticles. In addition, the RFR coating effectively mitigated nanoparticle aggregation in the CPA solution under the alternating magnetic field, as evidenced by the comparable SAR values of Fe<sub>3</sub>O<sub>4</sub>@RFR in VS55 and water. The presence of organic solvents and salts in VS55 did not affect the heating performance of the sample, which continued to exhibit a high SAR value in this colloidally challenging solution (Figure S7). The RFR layer enhances the colloidal stability of the nanoparticles, ensuring their uniform dispersion within the CPA solution, which is critical for achieving uniform nanowarming and for applications where the nanoparticles may

be perfused with solutions through the vasculature for whole organ cryopreservation and nanowarming. As such, the RFR coating helps maintain the rapid and uniform heating of the nanoparticles, which could be beneficial for subsequent nanowarming applications.

We further evaluated the heating performance of Fe<sub>3</sub>O<sub>4</sub>@ RFR at cryogenic temperatures with varying RFR thicknesses. Without magnetic nanoparticles, the VS55 solution showed a considerably lower heating rate. In contrast, incorporating Fe<sub>3</sub>O<sub>4</sub>@RFR nanoparticles improved the average heating rate of the VS55 solution to 78 °C/min within the temperature range of ~-100 to -40 °C at a relatively low concentration particle concentration of 3 mg Fe/mL (Figure 4b,c) and can be increased to 175 °C/min as the concentration increased to 10 mg Fe/mL (Figure 4d and Figure S8). Additionally, the heating curves for various sample concentrations suggested that the concentration of Fe<sub>3</sub>O<sub>4</sub>@RFR should exceed 1 mg of Fe/mL to achieve a sufficiently high heating rate to prevent the devitrification of VS55 (i.e., critical warming rate >50 °C/ min). It is noteworthy that while increasing the particle concentration can enhance the heating rate, careful temperature monitoring and precise operation are required to avoid overheating, which could potentially damage biological samples.

The biocompatibility of Fe<sub>3</sub>O<sub>4</sub>@RFR nanoparticles was evaluated by using human dermal fibroblast (HDF) cells. Figure 5a showed that the viability of HDF cells, quantified using a Cell Titer Blue assay (see the Supporting Information for the protocol used), remained unaffected in the presence of Fe<sub>3</sub>O<sub>4</sub>@RFR nanoparticles, even at elevated concentrations reaching 10 mg of Fe/mL, with no statistically significant decrease in cell viability after 2 h of exposure. Furthermore, we adopted an established protocol to investigate the cytotoxicity of stepwise loading and unloading of Fe<sub>3</sub>O<sub>4</sub>@RFR nanoparticles within the VS55 medium. 15,41 This procedure involved sequentially exposing HDF cells to incrementally varying concentrations of VS55, introducing the nanoparticles at peak concentrations and subsequently reducing the VS55 concentration, which simulates the exposure that might be expected during a nanowarming cryopreservation protocol. Notably, while the stepwise exposure to VS55 marginally reduced HDF cell viability to 90%, attributed to the inherent cytotoxicity of concentrated VS55, the incorporation of Fe<sub>3</sub>O<sub>4</sub>@RFR nanoparticles did not result in a further decrease in cell viability (Figure 5b). In addition, the live/dead cell assay results demonstrated that little or no visible cell death was observed after loading 10 mg of Fe/mL of Fe<sub>3</sub>O<sub>4</sub>@RFR directly into the cell culture medium or the VS55 medium (Figure 5c).

Furthermore, we applied Fe<sub>3</sub>O<sub>4</sub>@RFR nanoparticles to tissue cryopreservation. Porcine common iliac arteries (1.5 mm thick) were selected as the model system due to the clinical significance of arterial grafts. The ability to long-term bank arteries can be beneficial for transplant surgeries. Prior nanowarming attempts with EMG308 were successful for thinner porcine carotid arteries (1 mm thick) but faced challenges with thicker tissues. <sup>10,15</sup> Figure S9 shows the CPA loading and removal protocol of the arteries where a stepwise fashion was applied to reduce the osmotic shock. The diffusion model revealed that the center of the arteries is poorly loaded and therefore requires a higher warming rate to avoid devitrification. <sup>49</sup> Extending the loading time can enhance the loading amount but at the risk of increased toxicity. Therefore,

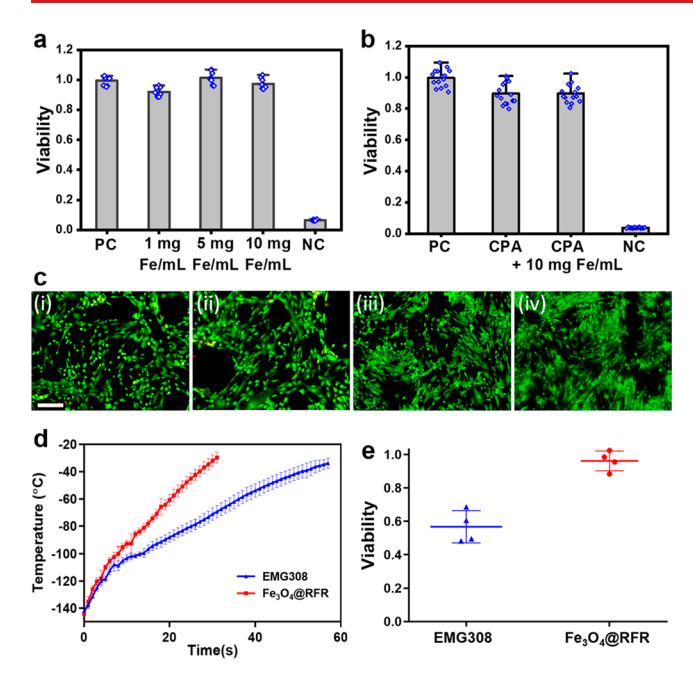


**Figure 5.** (a, b) Viability of HDF cells (a) in the presence of varying Fe<sub>3</sub>O<sub>4</sub>@RFR concentrations and (b) which underwent stepwise loading and unloading of VS55 with or without Fe<sub>3</sub>O<sub>4</sub>@RFR. Abbreviations: PC, positive control, representing fresh HDF cells in nanoparticle-free culture media; NC, negative control, devoid of cells. (c) Representative live (green)/dead (red) cell assay images of HDF cells under various conditions: (i) without Fe<sub>3</sub>O<sub>4</sub>@RFR; (ii) with 10 mg of Fe/mL of Fe<sub>3</sub>O<sub>4</sub>@RFR; (iii) after stepwise loading and unloading of VS55 without Fe<sub>3</sub>O<sub>4</sub>@RFR, and (iv) with 10 mg of Fe/mL of Fe<sub>3</sub>O<sub>4</sub>@RFR. The figures share the same scale bar: 150  $\mu$ m. (d) Warming profiles of EMG308 and Fe<sub>3</sub>O<sub>4</sub>@RFR during nanowarming of porcine iliac arteries. (e) Viability of iliac arteries after vitrification and nanowarming using EMG308 or Fe<sub>3</sub>O<sub>4</sub>@RFR (n = 4 for each group).

improving the intrinsic heating efficiency of the nanowarming agents is crucial. Figure S10 depicts the required warming rates for different loading times (15–25 min for each step) of VS55, and the achievable warming rates by nanowarming using two different particles (EMG308 and Fe<sub>3</sub>O<sub>4</sub>@RFR; warming profiles shown in Figure 5d). For a 20 min step loading, our model predicted the successful rewarming using Fe<sub>3</sub>O<sub>4</sub>@RFR nanoparticles due to their high heating efficiency, which was confirmed by the experimental viability outcomes shown in Figure 5e. Compared to commercial EMG308 nanoparticles, nanowarming with Fe<sub>3</sub>O<sub>4</sub>@RFR exhibited significantly enhanced viability. This result represents the first successful vitrification and nanowarming of a 1.5 mm thick iliac artery using nanoparticles.

In summary, we have demonstrated the rational design, size optimization, and surface modification of magnetic nanoclusters that are tailored for efficient nanowarming applications. Systematic investigation revealed that nanoclusters measuring 58 nm in diameter exhibit an ideal size for magnetic heating, achieving a high specific absorption rate surpassing commercial benchmarks. Surface modification with a permeable RFR polymer layer significantly enhanced the long-term colloidal stability of the nanoclusters in CPA solutions while maintaining an excellent heating performance. The nanoclusters enabled rapid heating of vitrified solutions at an average rate of 78 °C/min at a relatively low concentration of 3 mg Fe/mL. Cytotoxicity assays suggested biocompatibility of

the Fe<sub>3</sub>O<sub>4</sub>@RFR nanoparticles. Further, these nanoparticles were successfully applied to nanowarming of a 1.5 mm thick iliac artery. This integrated nanomaterial platform combining ideal magnetothermal properties, biostability, and biocompatibility represents a significant advance toward practical magnetic nanoparticle-assisted nanowarming techniques, paving the way for the subsequent phase of nanowarming intricate tissues or organs, as well as other emerging biomedical thermal therapies. 17,50,51 Additionally, the straightforward solvothermal conditions allow large-batch synthesis in bigger autoclaves, and the mild aqueous RFR polymerization has been implemented to generate gram quantities of tailored nanoparticles. 52,53 This tunable and scalable wet chemistry approach enables the gramscale production required for nanowarming applications for organs, making it an attractive platform for producing tailored magnetic nanoclusters as nanoscale heaters across scales. Beyond its immediate implications, our work establishes a versatile foundation for the tailored engineering of magnetic nanoparticles, empowering us to finely calibrate these nanoparticles to meet the unique demands of specific applications encompassing physical, chemical, and biological considerations.

## ASSOCIATED CONTENT

# Supporting Information

The Supporting Information is available free of charge at https://pubs.acs.org/doi/10.1021/acs.nanolett.4c00721.

Experimental details, TEM images, heating profiles, UV-vis spectra, summary of basic information on Fe<sub>3</sub>O<sub>4</sub>, and composition of VS55 CPA solution (PDF)

## AUTHOR INFORMATION

## **Corresponding Author**

Yadong Yin — Department of Chemistry, University of California, Riverside, California 92521, United States; orcid.org/0000-0003-0218-3042; Email: yadong.yin@ucr.edu

#### **Authors**

Zuyang Ye – Department of Chemistry, University of California, Riverside, California 92521, United States
 Youyi Tai – Department of Bioengineering, University of California, Riverside, California 92521, United States
 Zonghu Han – Department of Mechanical Engineering, University of Minnesota, Minneapolis, Minnesota 55455, United States

Sangmo Liu — Department of Chemistry, University of California, Riverside, California 92521, United States Michael L. Etheridge — Department of Mechanical Engineering, University of Minnesota, Minneapolis, Minnesota 55455, United States

Jacqueline L. Pasek-Allen – Department of Biomedical Engineering, University of Minnesota, Minneapolis, Minnesota 55455, United States

Chaitanya Shastry – Department of Chemistry, University of California, Riverside, California 92521, United States

Yun Liu – Department of Chemistry, University of California, Riverside, California 92521, United States

Zhiwei Li — Department of Chemistry, University of California, Riverside, California 92521, United States Chen Chen — Department of Chemistry, University of California, Riverside, California 92521, United States

- **Zhongxiang Wang** Department of Chemistry, University of California, Riverside, California 92521, United States;
  orcid.org/0009-0004-4870-0767
- John C. Bischof Department of Mechanical Engineering, University of Minnesota, Minneapolis, Minnesota 55455, United States; Department of Biomedical Engineering, University of Minnesota, Minneapolis, Minnesota 55455, United States; orcid.org/0000-0001-6726-7111
- Jin Nam Department of Bioengineering, University of California, Riverside, California 92521, United States; orcid.org/0000-0001-5117-8958

Complete contact information is available at: https://pubs.acs.org/10.1021/acs.nanolett.4c00721

#### **Author Contributions**

Z.Y., Z.L., and Y.Y. designed the project. Z.Y., S.L., C.S., and Y.L. synthesized and characterized the materials. C.C. and Z.W. helped with the characterization of nanoparticles and data analysis. M.L.E., J.L.P.-A., and J.C.B. contributed to the design of magnetic heating experiments and data analysis. Y.T. and J.N. designed and conducted the cell experiments. Z.H. conducted the nanowarming experiment of tissues. Z.Y. and Y.T. wrote the manuscript. M.L.E., J.C.B., J.N., and Y.Y. revised the manuscript. All authors have approved the final version of the manuscript.

#### Notes

The authors declare no competing financial interest.

#### ACKNOWLEDGMENTS

The authors are grateful for the financial support from the U.S. National Science Foundation under Grant No. EEC 1941543.

# **■** REFERENCES

- (1) Huang, H.; He, X.; Yarmush, M. L. Advanced technologies for the preservation of mammalian biospecimens. *Nat. Biomed. Eng.* **2021**, *5*, 793–804.
- (2) Murray, K. A.; Gibson, M. I. Chemical approaches to cryopreservation. *Nat. Rev. Chem.* **2022**, *6*, 579–593.
- (3) de Haan, M. J. A.; Rabelink, T. J. Cryopreservation breaks the organ transplant time barrier. *Nat. Rev. Nephrol.* **2023**, *19*, 623–624.
- (4) Sampaio-Pinto, V.; Janssen, J.; Chirico, N.; Serra, M.; Alves, P. M.; Doevendans, P. A.; Voets, I. K.; Sluijter, J. P. G.; van Laake, L. W.; van Mil, A. A Roadmap to Cardiac Tissue-Engineered Construct Preservation: Insights from Cells, Tissues, and Organs. *Adv. Mater.* **2021**, *33*, No. e2008517.
- (5) Bai, B. Y.; Xue, C. C.; Wen, Y.; Lim, J.; Le, Z. C.; Shou, Y. F.; Shin, S.; Tay, A. Cryopreservation in the Era of Cell Therapy: Revisiting Fundamental Concepts to Enable Future Technologies. *Adv. Funct. Mater.* **2023**, *33*, 2303373.
- (6) Zhan, L.; Rao, J. S.; Sethia, N.; Slama, M. Q.; Han, Z.; Tobolt, D.; Etheridge, M.; Peterson, Q. P.; Dutcher, C. S.; Bischof, J. C.; Finger, E. B. Pancreatic islet cryopreservation by vitrification achieves high viability, function, recovery and clinical scalability for transplantation. *Nat. Med.* **2022**, *28*, 798–808.
- (7) Chang, T.; Zhao, G. Ice Inhibition for Cryopreservation: Materials, Strategies, and Challenges. *Adv. Sci.* **2021**, *8*, 2002425.
- (8) Ma, Y.; Gao, L.; Tian, Y.; Chen, P.; Yang, J.; Zhang, L. Advanced biomaterials in cell preservation: Hypothermic preservation and cryopreservation. *Acta Biomater.* **2021**, *131*, 97–116.
- (9) Cao, Y.; Zhao, G.; Panhwar, F.; Zhang, X.; Chen, Z.; Cheng, L.; Zang, C.; Liu, F.; Zhao, Y.; He, X. The Unusual Properties of Polytetrafluoroethylene Enable Massive-Volume Vitrification of Stem Cells with Low-Concentration Cryoprotectants. *Adv. Mater. Technol.* **2019**, *4*, 1800289.

- (10) Han, Z.; Sharma, A.; Gao, Z.; Carlson, T. W.; O'Sullivan, M. G.; Finger, E. B.; Bischof, J. C. Diffusion Limited Cryopreservation of Tissue with Radiofrequency Heated Metal Forms. *Adv. Healthc. Mater.* **2020**, *9*, No. e2000796.
- (11) Huang, J.; Guo, J.; Zhou, L.; Zheng, G.; Cao, J.; Li, Z.; Zhou, Z.; Lei, Q.; Brinker, C. J.; Zhu, W. Advanced Nanomaterials-Assisted Cell Cryopreservation: A Mini Review. ACS Appl. Bio. Mater. 2021, 4, 2996–3014.
- (12) Zhan, L.; Han, Z.; Shao, Q.; Etheridge, M. L.; Hays, T.; Bischof, J. C. Rapid joule heating improves vitrification based cryopreservation. *Nat. Commun.* **2022**, *13*, 6017.
- (13) Han, H.; Zhan, T.; Cui, M.; Guo, N.; Dang, H.; Yang, G.; Shu, S.; He, W.; Xu, Y. Investigation of Rapid Rewarming Chips for Cryopreservation by Joule Heating. *Langmuir* **2023**, *39*, 11048–11062.
- (14) Wang, J.; Zhao, G.; Zhang, Z.; Xu, X.; He, X. Magnetic induction heating of superparamagnetic nanoparticles during rewarming augments the recovery of hUCM-MSCs cryopreserved by vitrification. *Acta Biomater.* **2016**, *33*, 264–274.
- (15) Manuchehrabadi, N.; Gao, Z.; Zhang, J.; Ring, H. L.; Shao, Q.; Liu, F.; McDermott, M.; Fok, A.; Rabin, Y.; Brockbank, K. G.; Garwood, M.; Haynes, C. L.; Bischof, J. C. Improved tissue cryopreservation using inductive heating of magnetic nanoparticles. *Sci. Transl. Med.* **2017**, *9*, No. eaah4586.
- (16) Liu, X.; Zhao, G.; Chen, Z.; Panhwar, F.; He, X. Dual Suppression Effect of Magnetic Induction Heating and Microencapsulation on Ice Crystallization Enables Low-Cryoprotectant Vitrification of Stem Cell-Alginate Hydrogel Constructs. ACS Appl. Mater. Interfaces 2018, 10, 16822–16835.
- (17) Kwizera, E. A.; Stewart, S.; Mahmud, M. M.; He, X. Magnetic Nanoparticle-Mediated Heating for Biomedical Applications. *J. Heat Transfer* **2022**, *144*, 030801.
- (18) Etheridge, M. L.; Xu, Y.; Rott, L.; Choi, J.; Glasmacher, B.; Bischof, J. C. RF heating of magnetic nanoparticles improves the thawing of cryopreserved biomaterials. *Technology* **2014**, *02*, 229–242.
- (19) Chiu-Lam, A.; Staples, E.; Pepine, C. J.; Rinaldi, C. Perfusion, cryopreservation, and nanowarming of whole hearts using colloidally stable magnetic cryopreservation agent solutions. *Sci. Adv.* **2021**, *7*, No. eabe3005.
- (20) Zhan, T.; Liu, K.; Yang, J.; Dang, H.; Chen, L.; Xu, Y. Fe<sub>3</sub>O<sub>4</sub> Nanoparticles with Carboxylic Acid Functionality for Improving the Structural Integrity of Whole Vitrified Rat Kidneys. *ACS Appl. Nano Mater.* **2021**, *4*, 13552–13561.
- (21) Tian, C.; Shen, L.; Gong, C.; Cao, Y.; Shi, Q.; Zhao, G. Microencapsulation and nanowarming enables vitrification cryopreservation of mouse preantral follicles. *Nat. Commun.* **2022**, *13*, 7515.
- (22) Han, Z.; Rao, J. S.; Gangwar, L.; Namsrai, B. E.; Pasek-Allen, J. L.; Etheridge, M. L.; Wolf, S. M.; Pruett, T. L.; Bischof, J. C.; Finger, E. B. Vitrification and nanowarming enable long-term organ cryopreservation and life-sustaining kidney transplantation in a rat model. *Nat. Commun.* **2023**, *14*, 3407.
- (23) Sharma, A.; Lee, C. Y.; Namsrai, B. E.; Han, Z.; Tobolt, D.; Rao, J. S.; Gao, Z.; Etheridge, M. L.; Garwood, M.; Clemens, M. G.; Bischof, J. C.; Finger, E. B. Cryopreservation of Whole Rat Livers by Vitrification and Nanowarming. *Ann. Biomed. Eng.* **2023**, *51*, 566–577.
- (24) Shore, D.; Ghemes, A.; Dragos-Pinzaru, O.; Gao, Z.; Shao, Q.; Sharma, A.; Um, J.; Tabakovic, I.; Bischof, J. C.; Stadler, B. J. H. Nanowarming using Au-tipped Co<sub>35</sub>Fe<sub>65</sub> ferromagnetic nanowires. *Nanoscale* **2019**, *11*, 14607–14615.
- (25) Pasek-Allen, J. L.; Wilharm, R. K.; Gao, Z.; Pierre, V. C.; Bischof, J. C. Phosphonate coating of commercial iron oxide nanoparticles for nanowarming cryopreserved samples. *J. Mater. Chem. B* **2022**, *10*, 3734–3746.
- (26) Fan, Q.; Li, Z.; Wu, C.; Yin, Y. Magnetically Induced Anisotropic Interaction in Colloidal Assembly. *Precis. Chem.* **2023**, *1*, 272–298.

- (27) Ye, Z.; Liu, S.; Yin, Y. Magnetic nanoparticles for nanowarming: seeking a fine balance between heating performance and biocompatibility. *Mater. Chem. Front.* **2023**, *7*, 3427–3433.
- (28) Jiang, K.; Liu, Y.; Pan, Y.; Wang, R.; Hu, P.; He, R.; Zhang, L.; Tong, G. Monodisperse Ni<sub>x</sub>Fe<sub>3-x</sub>O<sub>4</sub> nanospheres: Metal-ion-steered size/composition control mechanism, static magnetic and enhanced microwave absorbing properties. *Appl. Surf. Sci.* **2017**, *404*, 40–48.
- (29) Gavilan, H.; Simeonidis, K.; Myrovali, E.; Mazario, E.; Chubykalo-Fesenko, O.; Chantrell, R.; Balcells, L.; Angelakeris, M.; Morales, M. P.; Serantes, D. How size, shape and assembly of magnetic nanoparticles give rise to different hyperthermia scenarios. *Nanoscale* **2021**, *13*, 15631–15646.
- (30) Bertuit, E.; Benassai, E.; Meriguet, G.; Greneche, J. M.; Baptiste, B.; Neveu, S.; Wilhelm, C.; Abou-Hassan, A. Structure-Property-Function Relationships of Iron Oxide Multicore Nanoflowers in Magnetic Hyperthermia and Photothermia. *ACS Nano* **2022**, *16*, 271–284.
- (31) Gavilan, H.; Avugadda, S. K.; Fernandez-Cabada, T.; Soni, N.; Cassani, M.; Mai, B. T.; Chantrell, R.; Pellegrino, T. Magnetic nanoparticles and clusters for magnetic hyperthermia: optimizing their heat performance and developing combinatorial therapies to tackle cancer. *Chem. Soc. Rev.* **2021**, *50*, 11614–11667.
- (32) Gavilan, H.; Rizzo, G. M. R.; Silvestri, N.; Mai, B. T.; Pellegrino, T. Scale-up approach for the preparation of magnetic ferrite nanocubes and other shapes with benchmark performance for magnetic hyperthermia applications. *Nat. Protoc.* **2023**, *18*, 783–809.
- (33) Zhu, Y.; Zhao, W.; Chen, H.; Shi, J. A Simple One-Pot Self-Assembly Route to Nanoporous and Monodispersed Fe<sub>3</sub>O<sub>4</sub> Particles with Oriented Attachment Structure and Magnetic Property. *J. Phys. Chem. C* **2007**, *111*, 5281–5285.
- (34) Biswas, S.; Arief, I.; Panja, S. S.; Bose, S. Electromagnetic screening in soft conducting composite-containing ferrites: the key role of size and shape anisotropy. *Mater. Chem. Front.* **2017**, *1*, 2574–2589.
- (35) Mohapatra, J.; Zeng, F.; Elkins, K.; Xing, M.; Ghimire, M.; Yoon, S.; Mishra, S. R.; Liu, J. P. Size-dependent magnetic and inductive heating properties of  $Fe_3O_4$  nanoparticles: scaling laws across the superparamagnetic size. *Phys. Chem. Chem. Phys.* **2018**, 20, 12879–12887.
- (36) Mehdaoui, B.; Meffre, A.; Carrey, J.; Lachaize, S.; Lacroix, L. M.; Gougeon, M.; Chaudret, B.; Respaud, M. Optimal Size of Nanoparticles for Magnetic Hyperthermia: A Combined Theoretical and Experimental Study. *Adv. Funct. Mater.* **2011**, *21*, 4573–4581.
- (37) Serantes, D.; Simeonidis, K.; Angelakeris, M.; Chubykalo-Fesenko, O.; Marciello, M.; Morales, M. d. P.; Baldomir, D.; Martinez-Boubeta, C. Multiplying Magnetic Hyperthermia Response by Nanoparticle Assembling. *J. Phys. Chem. C* **2014**, *118*, 5927–5934.
- (38) Ovejero, J. G.; Cabrera, D.; Carrey, J.; Valdivielso, T.; Salas, G.; Teran, F. J. Effects of inter- and intra-aggregate magnetic dipolar interactions on the magnetic heating efficiency of iron oxide nanoparticles. *Phys. Chem. Chem. Phys.* **2016**, *18*, 10954–10963.
- (39) Nemati, Z.; Alonso, J.; Rodrigo, I.; Das, R.; Garaio, E.; García, J. Á.; Orue, I.; Phan, M.-H.; Srikanth, H. Improving the Heating Efficiency of Iron Oxide Nanoparticles by Tuning Their Shape and Size. J. Phys. Chem. C 2018, 122, 2367–2381.
- (40) Ring, H. L.; Sharma, A.; Ivkov, R.; Bischof, J. C. The impact of data selection and fitting on SAR estimation for magnetic nanoparticle heating. *Int. J. Hyperth.* **2020**, *37*, 100–107.
- (41) Gao, Z.; Ring, H. L.; Sharma, A.; Namsrai, B.; Tran, N.; Finger, E. B.; Garwood, M.; Haynes, C. L.; Bischof, J. C. Preparation of Scalable Silica-Coated Iron Oxide Nanoparticles for Nanowarming. *Adv. Sci.* **2020**, *7*, 1901624.
- (42) Mehl, P. M. Nucleation and Crystal Growth in a Vitrification Solution Tested for Organ Cryopreservation by Vitrification. *Cryobiology* **1993**, *30*, 509–518.
- (43) Guo, S.-R.; Gong, J.-Y.; Jiang, P.; Wu, M.; Lu, Y.; Yu, S.-H. Biocompatible, Luminescent Silver@Phenol Formaldehyde Resin Core/Shell Nanospheres: Large-Scale Synthesis and Application for In Vivo Bioimaging. *Adv. Funct. Mater.* **2008**, *18*, 872–879.

- (44) Chen, J.; Gong, M.; Fan, Y.; Feng, J.; Han, L.; Xin, H. L.; Cao, M.; Zhang, Q.; Zhang, D.; Lei, D.; Yin, Y. Collective Plasmon Coupling in Gold Nanoparticle Clusters for Highly Efficient Photothermal Therapy. ACS Nano 2022, 16, 910–920.
- (45) Li, Z.; Meng, Z.; Tian, F.; Ye, Z.; Zhou, X.; Zhong, X.; Chen, Q.; Yang, M.; Liu, Z.; Yin, Y. Fast Fourier Transform-weighted Photoacoustic Imaging by In Vivo Magnetic Alignment of Hybrid Nanorods. *Nano Lett.* **2022**, 22, 5158–5166.
- (46) Yang, Y.; Song, X.; Yao, Y.; Wu, H.; Liu, J.; Zhao, Y.; Tan, M.; Yang, Q. Ultrasmall single micelle@resin core-shell nanocarriers as efficient cargo loading vehicles for in vivo biomedical applications. *J. Mater. Chem. B* **2015**, *3*, 4671–4678.
- (47) Zhou, S.; Bai, Y.; Xu, W.; Feng, J.; Wang, X.; Li, Z.; Yin, Y. Formation of resorcinol-formaldehyde hollow nanoshells through a dissolution-regrowth process. *Nanoscale* **2020**, *12*, 15460–15465.
- (48) Li, Z.; Ye, Z.; Han, L.; Fan, Q.; Wu, C.; Ding, D.; Xin, H. L.; Myung, N. V.; Yin, Y. Polarization-Modulated Multidirectional Photothermal Actuators. *Adv. Mater.* **2021**, *33*, No. e2006367.
- (49) Han, Z. H.; Bischof, J. C. Critical Cooling and Warming Rates as a Function of Cpa Concentration. *Cryoletters* **2020**, *41*, 185–193.
- (50) Jiang, K.; Zhang, L.; Bao, G. Magnetic Iron Oxide Nanoparticles for Biomedical Applications. *Curr. Opin. Biomed. Eng.* **2021**, *20*, 100330.
- (51) Zhang, L.; Zhao, S.; Zhou, X.; Jing, X.; Zhou, Y.; Wang, Y.; Zhu, Y.; Liu, X.; Zhao, Z.; Zhang, D.; Feng, L.; Chen, H. A Magnetic-Driven Multi-motion Robot with Position/Orientation Sensing Capability. *Research* 2023, 6, 0177.
- (52) Zhang, X.-B.; Tong, H.-W.; Liu, S.-M.; Yong, G.-P.; Guan, Y.-F. An improved Stöber method towards uniform and monodisperse Fe<sub>3</sub>O<sub>4</sub>@C nanospheres. *J. Mater. Chem. A* **2013**, *1*, 7488–7493.
- (53) Zhao, H.; Zhang, F.; Zhang, S.; He, S.; Shen, F.; Han, X.; Yin, Y.; Gao, C. Scalable synthesis of sub-100 nm hollow carbon nanospheres for energy storage applications. *Nano Res.* **2018**, *11*, 1822–1833.